Particle-in-cell simulations of electron energization in laser-driven magnetic reconnection

2016 New J. Phys. 18 013051

(http://iopscience.iop.org/1367-2630/18/1/013051)

New Journal of Physics
The open access journal at the forefront of physics

Deutsche Physikalische Gesellschaft DPG
IOP Institute of Physics

Published in partnership with: Deutsche Physikalische Gesellschaft and the Institute of Physics

OPEN ACCESS

RECEIVED
7 July 2015

REVISED
5 October 2015

ACCEPTED FOR PUBLICATION
23 November 2015

PUBLISHED
25 January 2016

PAPER

Particle-in-cell simulations of electron energization in laser-driven magnetic reconnection

San Lu[1,2], **Quanming Lu**[1], **Fan Guo**[3], **Zhengming Sheng**[4,5], **Huanyu Wang**[1] **and Shui Wang**[1]

[1] CAS Key Lab of Geospace Environment, University of Science and Technology of China, Hefei 230026, People's Republic of China
[2] State Key Laboratory of Space Weather, Chinese Academy of Sciences, Beijing 100190, People's Republic of China
[3] Los Alamos National Laboratory, Los Alamos, NM 87545, USA
[4] MoE Key Laboratory for Laser Plasmas and Department of Physics, Shanghai Jiao Tong University, Shanghai 200240, People's Republic of China
[5] SUPA, Department of Physics, University of Strathclyde, Glasgow G4 0NG, UK

E-mail: qmlu@ustc.edu.cn

Keywords: electron energization, magnetic reconnection, laser-produced plasmas

Abstract

Electrons can be energized during laser-driven magnetic reconnection, and the energized electrons form three super-Alfvénic electron jets in the outflow region (Lu *et al* 2014 *New J. Phys.* **16** 083021). In this paper, by performing two-dimensional particle-in-cell simulations, we find that the electrons can also be significantly energized before magnetic reconnection occurs. When two plasma bubbles with toroidal magnetic fields expand and squeeze each other, the electrons in the magnetic ribbons are energized through betatron acceleration due to the enhancement of the magnetic field, and an electron temperature anisotropy $T_{e\perp} > T_{e||}$ develops. Meanwhile, some electrons are trapped and bounced repeatedly between the two expanding/approaching bubbles and get energized through a Fermi-like process. The energization before magnetic reconnection is more significant (or important) than that during magnetic reconnection.

1. Introduction

Magnetic reconnection is a fundamental physical process in plasmas during which the topologies of magnetic field lines are rearranged and magnetic energy is converted to plasma kinetic energy [1–3]. Magnetic reconnection is widely believed to be responsible for various kinds of explosive phenomena in space and laboratory plasmas, such as solar flares [4–6], magnetospheric substorms [7–9], and sawtooth crashes in tokamaks [10, 11]. The generation of energetic electrons is considered to be one of the most important signatures in magnetic reconnection [12–14]. Generally, two-dimensional (2D) particle-in-cell (PIC) simulations show that electrons can be accelerated by the parallel electric field when they move towards the X-line [15–17], and get further accelerated in the vicinity of the X-line by the reconnection electric field [18, 19]. Moreover, Hoshino *et al* [20] suggest that the electrons can also be accelerated in the magnetic pileup region during the curvature and gradient drift motions after the acceleration in the vicinity of the X-line.

In addition to the above non-adiabatic acceleration mechanisms, adiabatic betatron acceleration and Fermi acceleration are also proposed to explain the generation of energetic electrons in plasmas, especially in geospace and astrophysical plasmas [21–27]. Betatron acceleration works on the magnetized electrons in the enhancing magnetic field. The enhancement of the magnetic field leads to the generation of the inductive electric field, and the magnetized electrons are thus accelerated in the perpendicular direction by the inductive electric field. In contrast, Fermi acceleration is mainly in the parallel direction during which the magnetized electrons gain energy though head-on collision with the magnetic field. The classic Fermi acceleration can also be comprehended through the second adiabatic invariant $J = \int_0^L v_{||} ds$ taken over a bounce orbit. When the orbit shrinks/contracts, the conservation of J leads to the increase of $v_{||}$.

Dedicated laboratory experiments have been conducted to study magnetic reconnection, for example, the Todai Spheromak-3 [28, 29], the Swarthmore Spheromak Experiment facility [30, 31], the Magnetic Reconnection Experiment [32, 33], and the Versatile Toroidal Facility [34, 35]. More recently, magnetic reconnection experiments in laser-produced high-energy-density plasmas have also been conducted with the OMEGA laser facility [36, 37] and the Vulcan laser facility at the Rutherford Appleton laboratory [38–40], which provide a new experimental platform to study magnetic reconnection. In the experiments, two (or more) plasma bubbles with high density ($\geqslant 10^{20}$ cm^{-3}) and high temperature (~ 1 keV) are generated by focusing two nanosecond-duration laser beams on a planar-target foil. During the laser-plasma interaction, nonparallel density and temperature gradients lead to the spontaneous formation of azimuthal magnetic fields around the laser focal spots [41]. The azimuthal $\nabla n_e \times \nabla T_e$ magnetic field is found on the order of megagauss (MG), and forms toroidal ribbons wrapping around the plasma bubbles. When the laser beams are close enough, the bubbles eventually encounter each other with magnetic fields of opposing signs, and magnetic reconnection will occur.

The laser-driven magnetic reconnection experiment has also been conducted to at the Shenguang-II (SG-II) laser facility [42]. Electrons energized up to MeVs are observed in the outflow region of the reconnection experiment, and three well-collimated high-speed electron jets are generated. By performing 2D PIC simulations, Lu *et al* [43] have investigated the formation of the three high-speed electron jets, which are super-Alfvénic in laser-produced plasma reconnection. During magnetic reconnection, electrons can be accelerated by the reconnection electric field in the vicinity of the X-line. These accelerated electrons move away from the X-line, forming the upper and lower super-Alfvénic electron jets. Meanwhile, electrons can also penetrate into the reconnection pileup region, gyrate in a semi-circle, and get accelerated by the inductive electric field in the pileup region. These accelerated electrons form the center super-Alfvénic electron jet.

In this paper, we further demonstrate that, before magnetic reconnection occurs, the electrons can be energized significantly through betatron and Fermi-like acceleration. The expansion and approach of the plasma bubbles play essential roles in the electron energization processes. The remainder of the paper is organized as follows. Section 2 describes the simulation model, section 3 presents the simulation results, and section 4 gives the summary and discussions.

2. Simulation model

The simulation model used in the present study is a 2D PIC model in which the electromagnetic fields are defined on grids and updated by solving Maxwell equations with a full explicit algorithm. The positions and velocities of the ions and electrons are advanced relativistically in the electromagnetic fields. A first-order weighting is employed for the particle shape factor. The parameters and geometry in the simulations are all in accordance with the SG-II experimental setup [42]. The initial configuration of the simulation system is two expanding semicircular plasma bubbles, similar to the previous PIC simulations by Fox *et al* [44, 45] and Lu *et al* [43, 46]. The simulation domain is a rectangular in the (x, z) plane with $-L_x \leqslant x \leqslant L_x$, and $-L_z \leqslant z \leqslant L_z$. The two semicircular bubbles are centered at $(0, -L_z)$ and $(0, L_z)$ respectively. Define the radius vectors from the center of each bubble, $\mathbf{r}^{(1)} = (x, z + L_z)$ and $\mathbf{r}^{(2)} = (x, z - L_z)$.

The initial density is $n_b + n^{(1)} + n^{(2)}$, where n_b is the background density, and the density contribution from each bubble $n^{(i)}$ $(i = 1, 2)$ is

$$n^{(i)} = \begin{cases} (n_0 - n_b)\cos^2\left(\dfrac{\pi r^{(i)}}{2L_n}\right) & \text{if } r^{(i)} < L_n, \\ 0 & \text{otherwise.} \end{cases} \tag{1}$$

Here L_n is the initial scale of the bubbles and n_0 is the initial peak bubble density. In the simulation, we choose $n_b = 0.2n_0$. The initial expansion velocity of the bubbles is $\mathbf{V}^{(1)} + \mathbf{V}^{(2)}$, where $\mathbf{V}^{(i)}$ $(i = 1, 2)$ is

$$\mathbf{V}^{(i)} = \begin{cases} V_0 \sin\left(\dfrac{\pi r^{(i)}}{L_n}\right)\hat{\mathbf{r}}^{(i)} & \text{if } r^{(i)} < L_n, \\ 0 & \text{otherwise,} \end{cases} \tag{2}$$

and V_0 is the initial expanding speed of the two semi-bubbles. The initial magnetic field is the sum of two toroidal ribbons $\mathbf{B}^{(1)} + \mathbf{B}^{(2)}$, with

Table 1. Shenguang-II experimental parameters [42].

Parameter		Reported or estimated values
Ions		Al
Average ionic charge	Z	$\sim$10
Peak electron density	n_{e0}	$\sim 5 \times 10^{20}$ cm^{-3}
Peak ion density	n_{i0}	$\sim 5 \times 10^{19}$ cm^{-3}
Plasma bubble scale	L_n	200 μm
Width of magnetic ribbon	$2L_B$	80 μm
Temperature	T_i, T_e	570 eV
Magnetic field	B_0	2 MG
Estimated inflow speed	V_0	5.4×10^5 m s^{-1}
Ion inertial length	$d_i = c/\omega_{pi}$	16.8 μm
Alfvén speed	v_A	1.2×10^5 m s^{-1}
Electron beta	β_e	2.9
Sound speed	$C_s = (\gamma Z T_e/m_i)^{1/2}$	1.8×10^5 m s^{-1}

Table 2. Simulation parameters.

Parameter	Simulation setup
m_i/m_e	100
T_{i0}, $T_{e0}/m_e c^2$	0.026
$[L_x \times L_z]/d_i$	25.6×12.8
$N_x \times N_z$	1024×512
$(\Delta x, \Delta z)/d_i$	0.05
$\Omega_i \Delta t$	0.0001
L_n/d_i	12
L_B/d_i	2
c/v_A	75
V_0/C_s	3
n_b/n_0	0.2
Particle number per cell at n_0	500
Total particle number per species	$\sim 8 \times 10^7$

$$\mathbf{B}^{(i)} = \begin{cases} B_0 \sin\left(\dfrac{\pi\left(L_n - r^{(i)}\right)}{2L_B}\right)\hat{\mathbf{r}}^{(i)} \times \hat{\mathbf{y}} & \text{if } r^{(i)} \in \left[L_n - 2L_B, L_n\right], \\ 0 & \text{otherwise,} \end{cases} \tag{3}$$

where B_0 is the magnitude of the initial magnetic field, and L_B is the half-width of the magnetic ribbons. To be consistent with the plasma flow, an initial electric field $\mathbf{E} = -\mathbf{V} \times \mathbf{B}$ is imposed, while the initial current density is determined by Ampere's law.

Table 1 lists the reported or otherwise estimated parameters for the SG-II experiment [42]. Table 2 lists the numerical parameters used in the simulations. The measured electron density near the X-line of reconnection is $\sim 5 \times 10^{19}$ cm^{-3}, which is on the order of one tenth of the peak electron density based on the simulations. The peak electron density is thus about 5×10^{20} cm^{-3}. Given the average ionic charge $Z \sim 10$, the peak ion density is about 5×10^{19} cm^{-3}. Therefore, the ion inertial length based on the peak ion density is $d_i = c/\omega_{pi} \approx 16.8$ μm. In the experiment, the radius of the plasma bubbles is about $L_n = 200$ μm, and the width of the magnetic ribbons is about $2L_B = 80$ μm. So in our simulation, we choose $L_n = 12d_i$ and $L_B = 2d_i$. As the plasma bubbles expand and squeeze each other, the magnetic field can be enhanced several times compared to the initial value. The enhanced magnetic field is measured to be about 3.75 MG in the experiment. Thus, we choose the initial magnetic field $B_0 = 2$ MG in the simulation. The mass ratio $m_i/m_e = 100$ and the light speed $c = 75v_A$, where v_A is the Alfvén speed based on B_0 and n_0. The initial velocity distributions for the ions and electrons are Maxwellian with bulk velocity in the radial direction and drift velocity in the out-of-plane

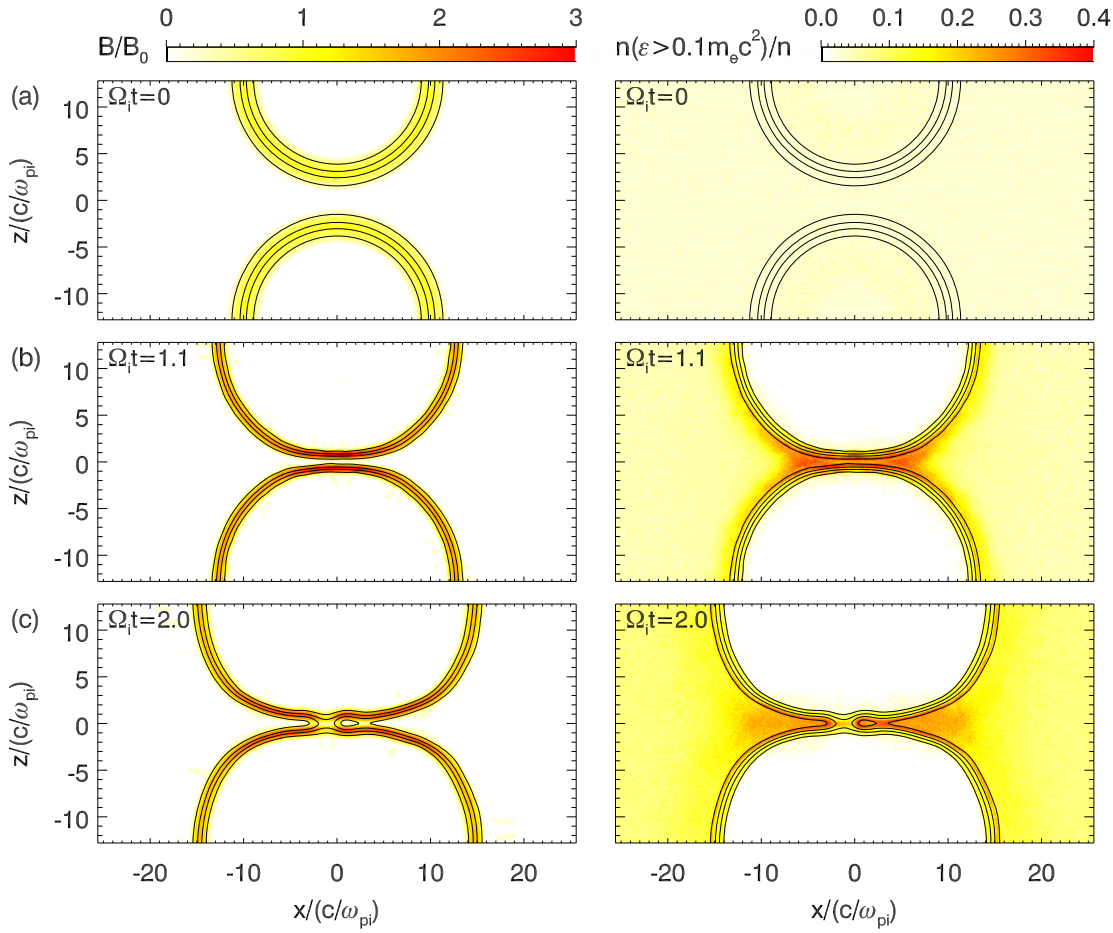

Figure 1. Magnetic field magnitude B/B_0 (left column) and the portion of the energetic electrons whose energy is larger than $0.1m_ec^2$ (right column), at $\Omega_i t =$ (a) 0, (b) 1.1, and (c) 2.0. The black curves denote the magnetic field lines in the (x, z) plane.

direction. Uniform ion and electron initial temperatures $T_i = T_e = 0.026m_ec^2$ are adopted for simplicity. The expansion speed of the plasma bubbles is on the order of the sound speed $C_s = (\gamma ZT_e/m_i)^{1/2}$. In the simulation, we choose the initial expanding speed $V_0 = 3C_s$. The cell dimensions are $N_x \times N_z = 1024\times512$, with the spatial resolution of $\Delta x = \Delta z = 0.05c/\omega_{pi} = 0.5c/\omega_{pe} = 3.125\lambda_{De}$, where λ_{De} is the electron Debye length. Therefore, $L_x = 25.6c/\omega_{pi}$ and $L_z = 12.8c/\omega_{pi}$. The time step is $\Delta t = 0.0001\Omega_i^{-1}$, where Ω_i is the ion gyrofrequency based on B_0. About 8×10^7 particles per species are employed to simulate the plasmas. Periodic boundary conditions are used in both the x and z directions.

In the simulations, we choose $c/v_A = 75$ which is larger than that in some other PIC simulations [27, 47] (nevertheless, it is still much smaller than the realistic value). Our purpose is to pick a small thermal speed in comparison to the speed of light. If the initial thermal speed is comparable to the speed of light, the electrons are thus already relativistic at the initial time, which is far from the realistic experimental setup. In PIC simulations, to accommodate the available computer resources, it is common to use a nonrealistic mass ratio (100 or even smaller), not only in the simulations of the geospace plasmas [27, 47], but also in the simulations of the plasmas in laboratory [45, 48]. The mass ratio $m_i/m_e = 100$ can distinguish the motions of the electrons and the ions well. The kinetic physics is not sensitive to the mass ratio qualitatively, so the energization mechanisms discussed in this paper do not change with different mass ratios.

3. Simulation results

Figure 1 shows magnetic field lines and contours of the magnetic field B/B_0 and the portion of the energetic electrons $n(\varepsilon > 0.1m_ec^2)/n$ (where n is the local electron density, and the energetic electrons are the electrons whose energy is larger than $0.1m_ec^2$) at $\Omega_i t =$ (a) 0, (b) 1.1, and (c) 2.0. Panel (a) gives the initial condition for the magnetic field (equation (3)). At the initial time, the portion of the energetic electrons is very low, about 5%. As the two plasma bubbles expand at a supersonic speed, they strongly squeeze each other, which piles up the magnetic flux in the inflow region before reconnection occurs. At $\Omega_i t = 1.1$, just before the beginning of the

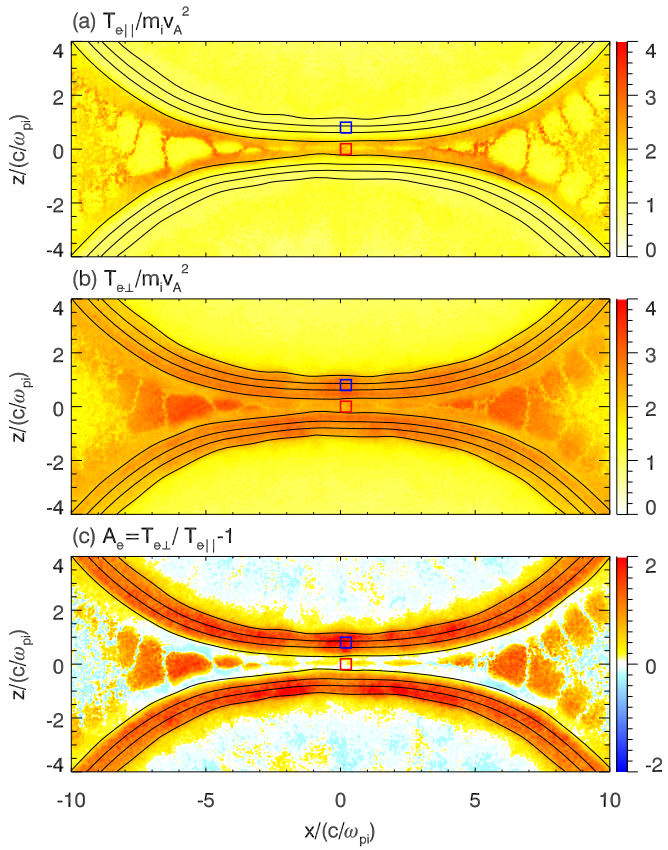

Figure 2. Electron (a) parallel temperature $T_{e||}/m_i v_A^2$, (b) perpendicular temperature $T_{e\perp}/m_i v_A^2$, and (c) temperature anisotropy $A_e = T_{e\perp}/T_{e||} - 1$ at $\Omega_i t = 1.1$. The corresponding magnetic field lines are also plotted.

reconnection, the upstream magnetic field is strongly enhanced, with a maximum of about $3B_0$. Meanwhile, a long and thin current sheet forms between the two plasma bubbles. The electrons are significantly energized, especially in the magnetic ribbons and the region between the two plasma bubbles. In these regions, nearly 40% of the electrons are energized to $\varepsilon > 0.1 m_e c^2$. At $\Omega_i t = 2.0$, two reconnection X-lines generates in the current sheet, and a plasmoid forms between the two X-lines. The portion of the energetic electrons is still high in the reconnection outflow region.

Figure 2 presents the electron (a) parallel temperature $T_{e||}/m_i v_A^2$, (b) perpendicular temperature $T_{e\perp}/m_i v_A^2$, and (c) temperature anisotropy $A_e = T_{e\perp}/T_{e||} - 1$ at $\Omega_i t = 1.1$. In the magnetic ribbons, a strong electron temperature anisotropy develops. In the region denoted by the blue box, the electron parallel temperature $T_{e||}/m_i v_A^2 \approx 1$, and the perpendicular temperature $T_{e\perp}/m_i v_A^2 \approx 3$. The corresponding temperature anisotropy is thus $A_e \approx 2$. From $\Omega_i t = 0$ to 1.1, the electrons are mainly heated in the perpendicular direction. Figure 3(a) shows the velocity distribution of the electrons in the blue box in figure 2. The red arrows denote the directions of the local magnetic field which is mainly along the x direction. The electron distribution is bi-Maxwellian with the perpendicular temperature higher than the parallel temperature. Figure 3(b) shows the velocity distribution of the accelerated electrons in the red box in figure 2. The velocity distribution is spread out mainly in the z direction, which indicates that the acceleration in the field reversal region is mainly in the v_z direction.

To further investigate the electron energization mechanism in the magnetic ribbons, we 'tag' the electrons in the blue box (see figure 2) at $\Omega_i t = 1.1$, and re-run the simulation to trace the positions and energies of the tagged electrons. Figure 4 presents the spatial and energy distributions of these tagged electrons at three different times, $\Omega_i t =$ (a) 0, (b) 0.5, and (c) 1.0. Initially, most of the electrons are located in the magnetic ribbons with the energy around the initial temperature $0.025 m_e c^2$. At $\Omega_i t = 0.5$, the electrons are energized, with the average energy of about $0.04 m_e c^2$. The average energy is further enhanced to about $0.07 m_e c^2$ at $\Omega_i t = 1.0$, and some of the electrons can be accelerated to higher energy, over $0.2 m_e c^2$. Note that the electron energization is accompanied by the magnetic field enhancement, and most of the energized electrons are magnetized in the magnetic ribbons, which suggest a process of betatron acceleration.

A representative electron, electron 1, is presented in figure 5 to further illustrate the electron betatron acceleration process in the compressed magnetic ribbons. Figures 5(a)–(c) show the trajectory of the electron during different time intervals. The background contours show the magnitude of the magnetic field, and the

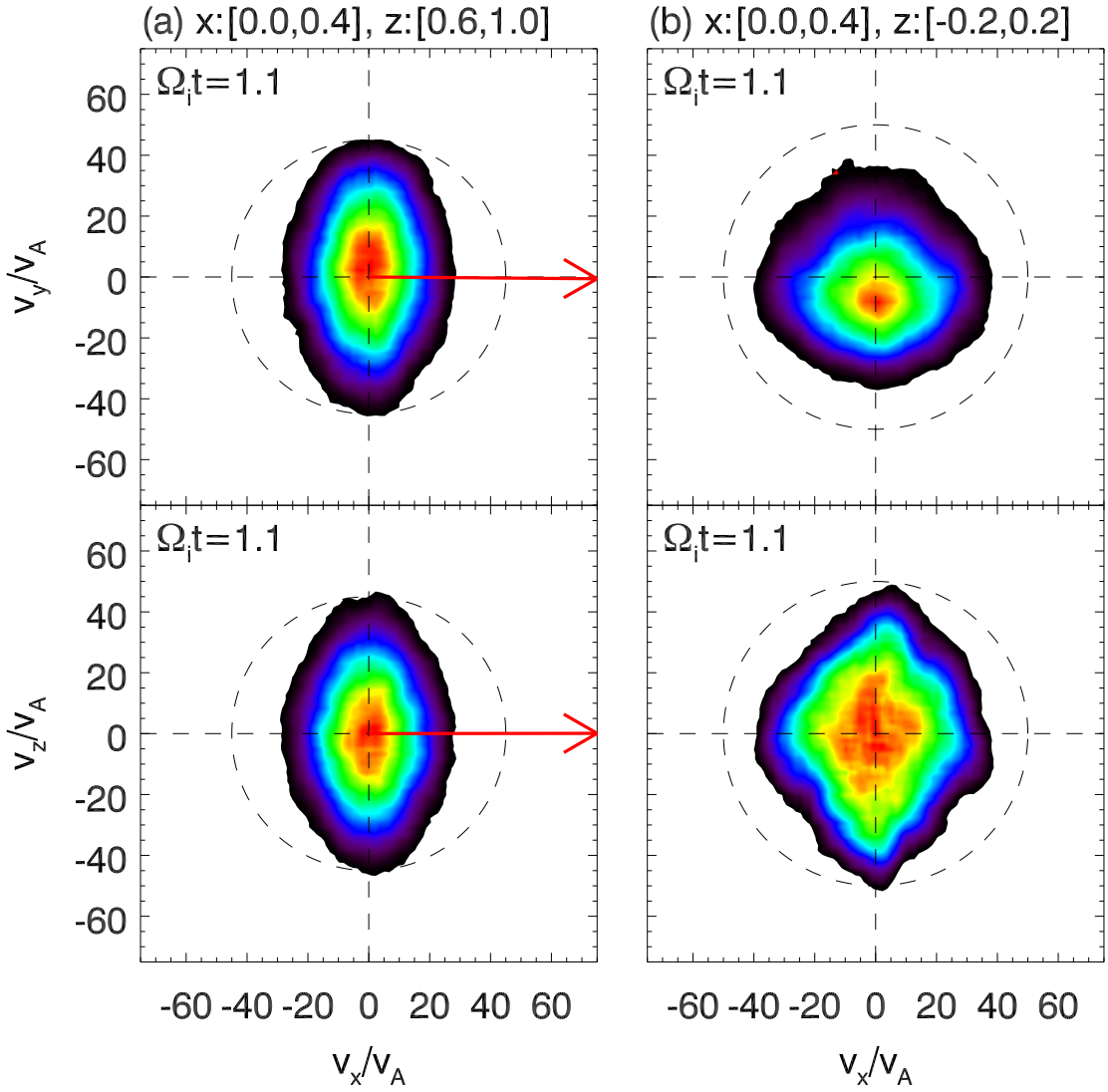

Figure 3. Electron velocity distributions $f(v_x, v_y)$ (top panel) and $f(v_x, v_z)$ (bottom panel) in (a) $x \in [0,0.4]c/\omega_{pi}$, $z \in [0.6,1]c/\omega_{pi}$, and (b) $x \in [0,0.4]c/\omega_{pi}$, $z \in [-0.2,0.2]c/\omega_{pi}$ at $\Omega_i t = 1.1$. The two regions are marked by blue and red rectangles, respectively, in figure 2. The red arrows denote the direction of the local magnetic field, and the dashed circles represent the isotropic distributions.

magnetic field lines are also plotted for reference. Figures 5(d) and (e) plot the time evolutions of the electron kinetic energy $\varepsilon/m_e c^2$ and magnetic moment $\mu B_0/m_e c^2$ respectively. It is easy to note that the electron is magnetized in the ribbons all the time from $\Omega_i t = 0$ to 1.1, during which the magnetic field is enhanced from B_0 to nearly $3B_0$. The electron is accelerated from about $0.03 m_e c^2$ to about $0.1 m_e c^2$, and the magnetic momentum of the electron is almost kept as a constant, $\mu B_0/m_e c^2 \approx 0.03$. The enhancement of the magnetic field leads to the generation of the inductive electric field in the magnetic ribbons, and the magnetized electrons are accelerated in the perpendicular direction by the inductive electric field. Therefore, electron 1 is energized through betatron acceleration, and this kind of energized electrons forms a bi-Maxwellian distribution with the electron temperature anisotropy ($T_{e\perp} > T_{e\parallel}$, see figure 3(a)).

In the magnetic field reversal region between the two expanding bubbles, the electrons can also be energized significantly, especially in the v_z direction (see figure 3(b)). We also trace the trajectories and energies of all the electrons in the red box (see figure 2) at $\Omega_i t = 1.1$. Figure 6 shows the positions and energies of these electrons at $\Omega_i t =$ (a) 0, (b) 0.5, and (c) 1.0. The electrons are initially located in the region outside of the plasma bubbles, namely the background region, with an averaged energy of about $0.025 m_e c^2$. As the expansion and compression of the two plasma bubbles, the electrons are accelerated at the edges of the magnetic ribbons. The averaged energy of the tagged electrons increases to about $0.035 m_e c^2$ at $\Omega_i t = 0.5$, and over $0.08 m_e c^2$ at $\Omega_i t = 1.0$. Some of the electrons can be accelerated to relativistic energy, over $0.4 m_e c^2$. Figures 7(a)–(c) show the orbit of a representative energetic electron, electron 2, for the time interval from $\Omega_i t = 0$ to 1.1. Figures 7(d) and (e) show the time evolutions of the kinetic energy and velocity of the electron respectively. The electron moves in the background region and bounces repeatedly between the two expanding bubbles. From $\Omega_i t = 0.4$ to 1.1,

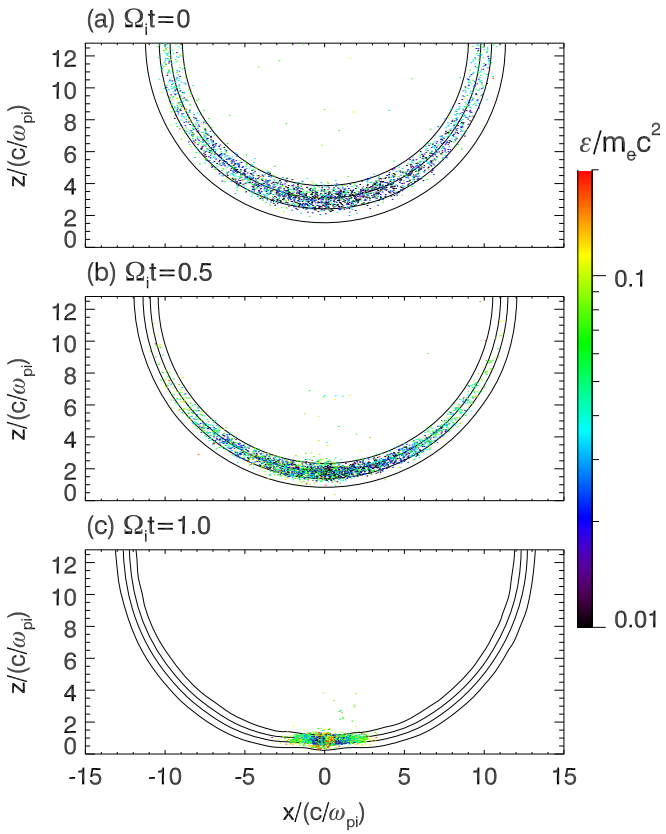

Figure 4. Positions of electrons are traced backward in time at $\Omega_i t =$ (a) 0, (b) 0.5, and (c) 1.0. The electrons are located in the blue rectangle in figure 2 at $\Omega_i t = 1.1$. The colors of the dots represent the kinetic energies $\varepsilon/m_e c^2$ for each electron. The plots are zoomed in on the upper plasma bubble to show the colored particles more clearly.

electron 2 is reflected sixteen times between the two plasma bubbles (or magnetic ribbons) in the z direction. During each of the reflections, the electron gains a larger absolute value of v_z. At the same time, the electron is accelerated in the $-y$ direction by the inductive electric field $E_y \approx VB$, where V is the radial expansion speed and B is the toroidal magnetic field. As the accumulation of this kind reflection, electron 2 is accelerated with the energy increases from about $0.1 m_e c^2$ to about $0.5 m_e c^2$. Figure 8 further shows the kinetic energy of electron 2 as a function of its z position. The electron gains energy as it is reflected by magnetic ribbons at the boundaries of the bubbles, which suggests that the energization process of electron 2 is a Fermi-like process.

The magnetic field shows a wavy structure along the toroidal direction (parallel to the magnetic field) of the compressed magnetic ribbons. Figure 9 depicts the zoomed-in structures of the magnetic field lines and the out-of-plane magnetic field B_y at $\Omega_i t =$ (a) 0.65, (b) 0.9, and (c) 1.8. At $\Omega_i t = 0.65$, B_y shows a wavy structure with alternate positive and negative values along the direction parallel to the magnetic field. The wavelength of the structure is about $2c/\omega_{pi}$. The wavy magnetic field perturbation grows stronger at $\Omega_i t = 0.9$ (see figure 9(b)). Besides the out-of-plane magnetic field B_y, the in-plane magnetic field (indicated by the magnetic field lines) is also wavy. At $\Omega_i t = 1.8$, due to the Hall effect of magnetic reconnection, there forms the quadrupolar structure of B_y. During the same time, the wavy magnetic field perturbation gradually decreases. At the edges of the magnetic ribbons, the magnetic field is weak and the electron temperature is anisotropic, which is favorable to the Weibel instability [49]. The wavy magnetic structure along the parallel direction is considered to be the consequence of the Weibel instability.

Figure 10 depicts the time evolution of B_y perturbation at the inner edge of the magnetic ribbons. After about $\Omega_i t = 0.3$, the wavy B_y grows up from the noises, and keeps growing until about $\Omega_i t = 0.7$ after which the B_y perturbation begins to saturate. The red dashed line shows an exponential fit to the growth stage, $B_y \sim \exp\left[\gamma_{sim}(t - t_0)\right]$, with the fitted growth rate $\gamma_{sim} \approx 5.1\Omega_i$, and $t_0 = 0.3\Omega_i^{-1}$ is the time when the wavy perturbation begins to grow. Based on the analytical theory [50], the Weibel instability occurs for wavelengths such that

$$k^2 \leqslant k_0^2 \equiv \frac{\omega_{pe}^2}{c^2}\left(\frac{T_{e\perp}}{T_{e\parallel}} - 1\right). \tag{4}$$

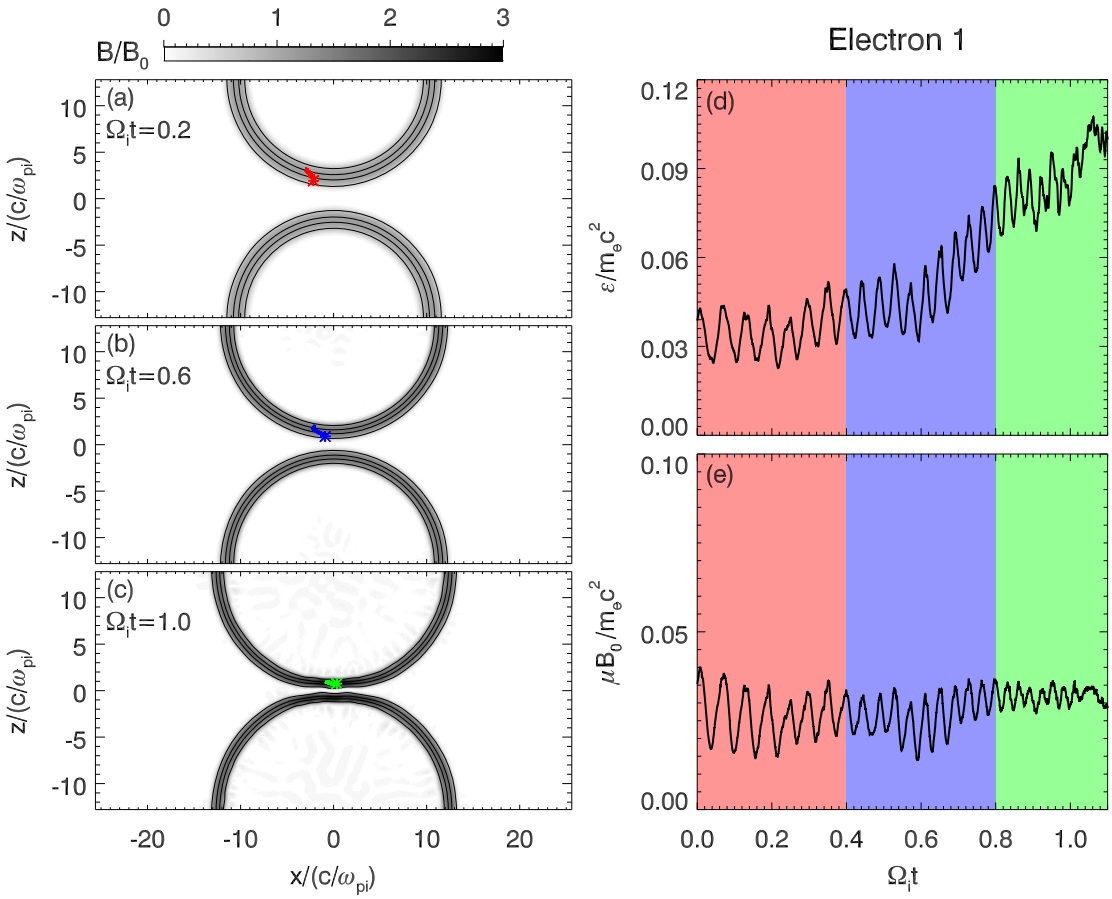

Figure 5. A representative betatron accelerated electron, electron 1. Panels (a)–(c) show the trajectory of electron 1 during (a) $0 \leqslant \Omega_i t \leqslant 0.4$, (b) $0.4 \leqslant \Omega_i t \leqslant 0.8$, and (c) $0.8 \leqslant \Omega_i t \leqslant 1.1$. The background images are the magnetic field magnitude B/B_0 at $\Omega_i t =$ (a) 0.2, (b) 0.6, and (c) 1.0. Panels (d) and (e) plot the time evolutions of the electron kinetic energy $\varepsilon/m_e c^2$ and magnetic momentum $\mu B_0/m_e c^2$ respectively.

The growth rate reaches its maximum at $k^2 = \frac{1}{3}k_0^2$, with

$$\gamma_{\max} = \left(\frac{8}{27\pi}\right)^{1/2} \omega_{pe} \left(\frac{T_{e\|}}{m_e c^2}\right)^{1/2} \frac{T_{e\|}}{T_{e\perp}} \left(\frac{T_{e\perp}}{T_{e\|}} - 1\right)^{3/2}, \tag{5}$$

where ω_{pe} is the electron plasma frequency. For $A_e = T_{e\perp}/T_{e\|} - 1 \approx 0.56$, $n_e \approx 0.4n_0$, $B \approx 0.3B_0$, $T_{e\perp} \approx 1.4m_i v_A^2$, and $T_{e\|} \approx 0.9m_i v_A^2$ as measured at the inner edge of the magnetic ribbons where the instability is excited at $\Omega_i t = 0.3$, based on the above analytical theory, the maximum growth rate is estimated as $\gamma_{th} \approx 5.3\Omega_i$, and the wave number $k \approx 2.7\omega_{pi}/c$, corresponding to the wavelength $\lambda \approx 2.3c/\omega_{pi}$. The wavelength obtained in the simulation is found to be consistent with the analytical theory, and the growth rate $\gamma_{sim} \approx 5.1\Omega_i$ is also close to the analytical γ_{th}. The above consistency between the simulation and linear theory shows that the formation of the wavy B_y perturbation is due to the Weibel instability driven by the electron temperature anisotropy.

After about $\Omega_i t = 1.1$, magnetic reconnection begins, and the electrons are further energized. Figure 11 shows the contour of the electron bulk velocity V_{ex}/v_A at $\Omega_i t = 2.6$ and two representative electrons (electrons 3 and 4) that are accelerated during the reconnection process. At $\Omega_i t = 1.8$, electron 3 has been accelerated to about $0.1m_e c^2$ through betatron acceleration in the magnetic ribbons. In the vicinity of the X-line (or electron diffusion region), the magnetic field is weak. The electron moves towards the X-line due to the magnetic mirror force $\mathbf{F} = \mu\nabla B$. Once the electron moves into the electron diffusion region, the electron is accelerated by the reconnection electric field E_y therein from $\Omega_i t = 2.0$ to $\Omega_i t = 2.2$. After $\Omega_i t = 2.2$, the accelerated electron 3 then leaves the X-line along magnetic field lines. Background electrons can also be accelerated in the magnetic pileup region of the reconnection. During $2.5 \leqslant \Omega_i t \leqslant 2.64$, a background electron (electron 4) moves towards the reconnection pileup region with a relatively lower energy. The magnetic field in the background region is very weak, so there is a sharp boundary between the background region and the pileup region. At about $\Omega_i t = 2.64$, the electron penetrates through the boundary and moves into the pileup region. In the pileup region, it senses a $\mathbf{v}_e \times \mathbf{B}$ Lorentz force, which causes it to gyrate for about half an orbit. At the same time, the

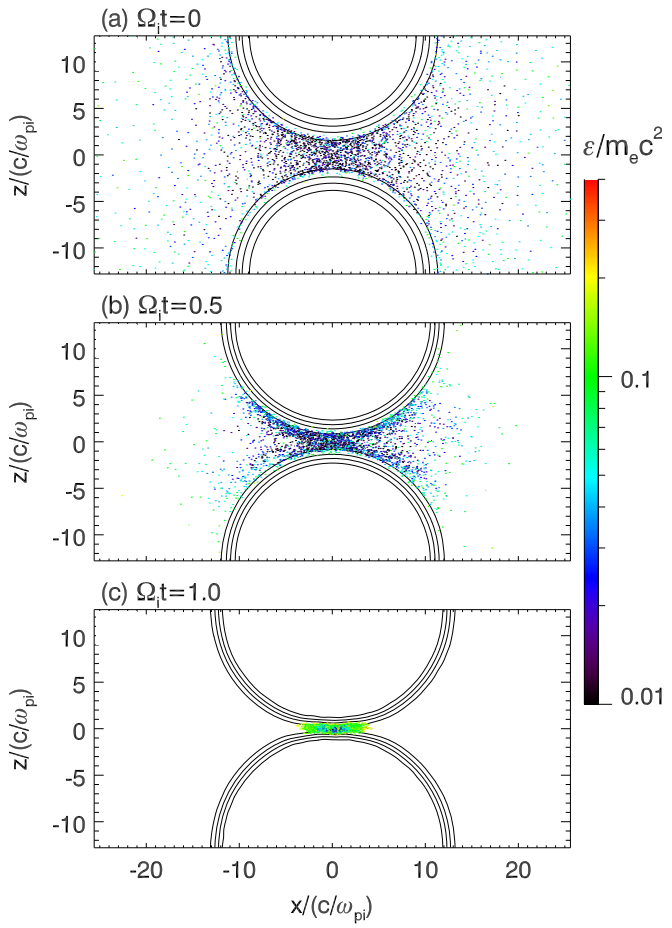

Figure 6. Backtrace of the electrons located in the red rectangle in figure 2 at $\Omega_i t = 1.1$. Same format as figure 4.

electron is accelerated in the y direction by the inductive electric field E_y in the pileup region. At about $\Omega_i t = 2.68$, after the semi-cycle, the electron leaves the pileup region and moves back into the background region along the $-x$ direction with a higher energy of about $0.48 m_e c^2$.

Figure 12 plots the electron energy spectra in the whole simulation domain at $\Omega_i t = 0$, 1.1, and 2.0. At the initial time, the electron distribution is Maxwellian with a temperature of about $0.025 m_e c^2$. At $\Omega_i t = 1.1$ just before the reconnection begins, the electrons are strongly heated/accelerated through betatron and Fermi-like processes, with the high energy part extends beyond $0.4 m_e c^2$. After the beginning of magnetic reconnection, at $\Omega_i t = 2.0$, the electrons are further energized by the reconnection process. Note that the energization through betatron and Fermi-like processes before magnetic reconnection is more significant than the energization by magnetic reconnection.

Time evolutions of total energy $\varepsilon_{\rm total}$, ion kinetic energy $\varepsilon_{\rm i}$, electron kinetic energy $\varepsilon_{\rm e}$, and magnetic energy $\varepsilon_{\rm B}$ are shown in figure 13. It is noted that the total energy is well conserved in the simulations. Based on the energy evolutions, the whole process of the laser-driven reconnection can be summarized as follows: the initial supersonic expansion of the plasma bubbles leads to the enhancement of the magnetic field, and the electrons are energized through betatron and Fermi-like processes. Therefore, at the early stage, the ion kinetic energy is converted to the magnetic energy and electron kinetic energy. At the second stage after magnetic reconnection begins, the increase of the magnetic energy slows down due to the dissipation caused by reconnection. At the last stage, the expansion of the bubbles is gradually stopped, reconnection becomes the dominant process. The magnetic energy is converted to the kinetic energies of the electrons and ions through magnetic reconnection.

4. Conclusions and discussion

In this paper, based on the geometry and parameters of the SG-II reconnection experiment, we performed 2D PIC simulations to investigate the electron energization in laser-driven magnetic reconnection. The electrons were found to be energized to high energy before magnetic reconnection occurs, and the following magnetic reconnection can further energize these electrons. The energization before magnetic reconnection is more

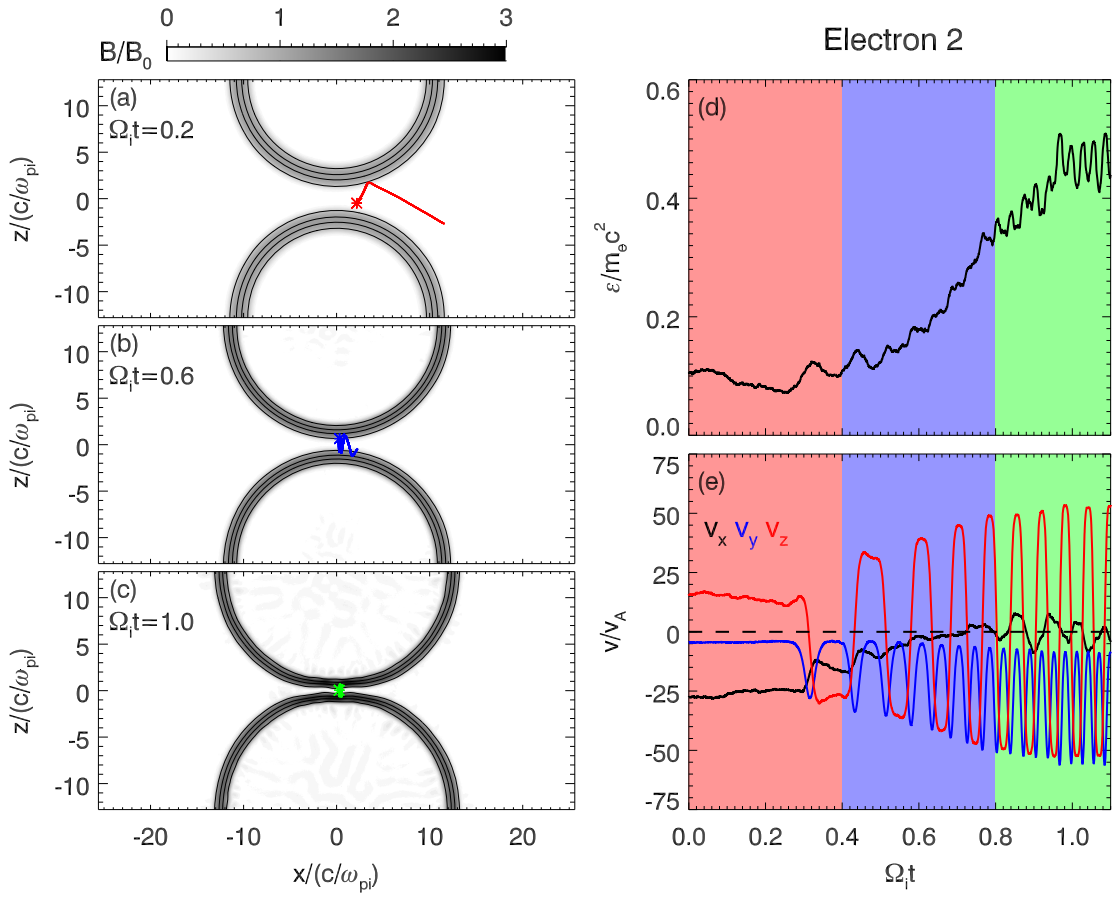

Figure 7. A representative Fermi-like accelerated electron, electron 2. Panels (a)–(c) show the trajectory of electron 2 during (a) $0 \leqslant \Omega_i t \leqslant 0.4$, (b) $0.4 \leqslant \Omega_i t \leqslant 0.8$, and (c) $0.8 \leqslant \Omega_i t \leqslant 1.1$. The background images are the magnetic field magnitude B/B_0 at $\Omega_i t =$ (a) 0.2, (b) 0.6, and (c) 1.0. Panels (d) and (e) plot the time evolutions of the electron kinetic energy $\varepsilon/m_e c^2$ and velocity components v_x, v_y, and v_z respectively.

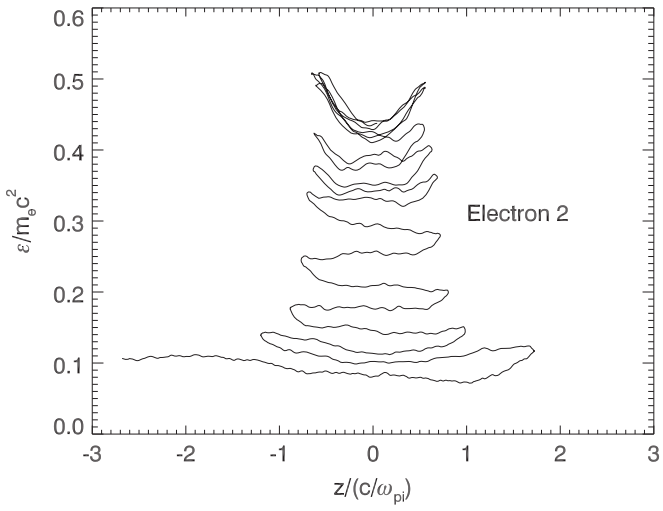

Figure 8. Kinetic energy of electron 2 as a function of its z position.

significant than that during magnetic reconnection. Before magnetic reconnection occurs, the magnetic field of the magnetic ribbons is enhanced due to the expansion of the plasma bubbles and the compression between the bubbles, which leads to the betatron acceleration of the electrons therein. The betatron acceleration is mainly in the perpendicular direction, therefore, an electron temperature anisotropy $T_{e\perp} > T_{e||}$ develops. The Weibel instability is excited by the electron temperature anisotropy, which generates a wavy magnetic structure at the

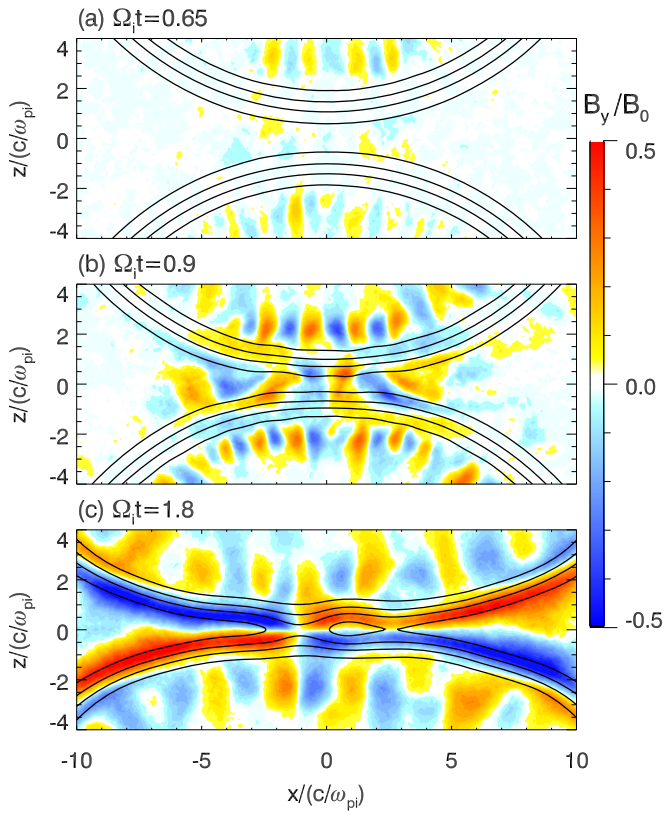

Figure 9. Out-of-plane magnetic field B_y/B_0 at $\Omega_i t =$ (a) 0.65, (b) 0.9, and (c) 1.8. The black curves denote the in-plane magnetic field lines.

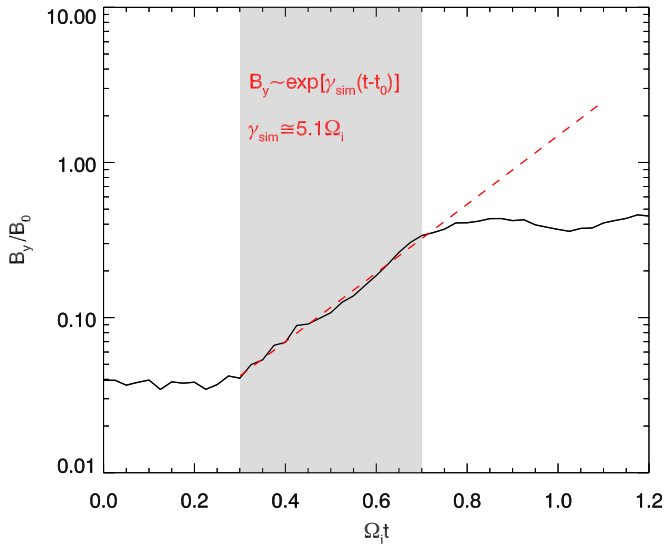

Figure 10. Time evolution of the magnetic field wavy perturbation B_y/B_0. At each time step, the amplitude of the wavy perturbation is defined as the maximum value of B_y/B_0 in the region $-5 < x/(c/\omega_{pi}) < 5$, $z/(c/\omega_{pi}) < -2$ or $z/(c/\omega_{pi}) > 2$. The gray area indicates the linear growth phase, and the dashed line shows an exponential fit, with the fitted growth rate obtained from the simulation $\gamma_{sim} \approx 5.1\Omega_i$.

edges of the magnetic ribbons. At the same time, some electrons can be bounced repeatedly between the two expanding bubbles and get energized through a Fermi-like process. After magnetic reconnection begins, the electrons are further energized. Part of the electrons can be accelerated by reconnection electric field in the vicinity of the X-line, and then move away from the X-line. Electrons can also be accelerated in the pileup region

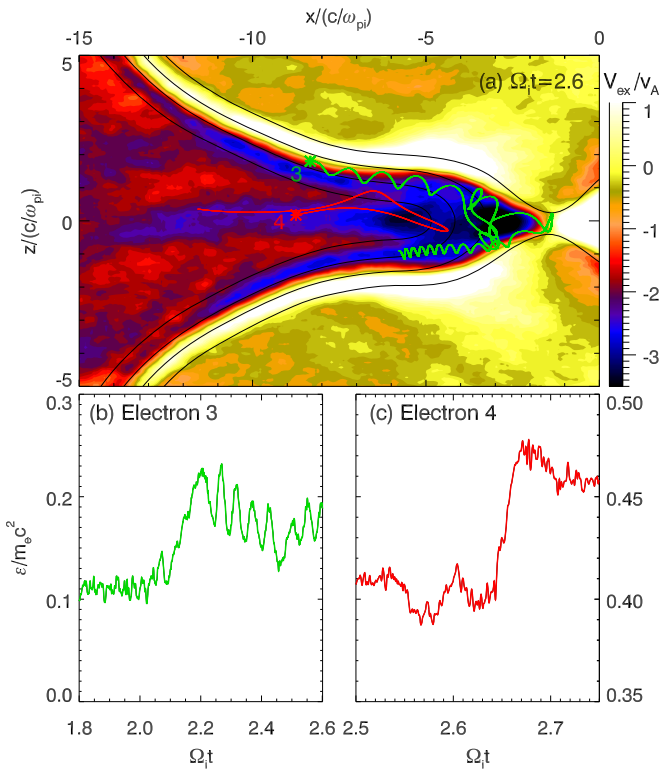

Figure 11. (a) Electron bulk velocity in the x direction V_{ex}/v_A at $\Omega_i t = 2.6$, and trajectories of electrons 3 (green) and 4 (red) during $1.8 \leqslant \Omega_i t \leqslant 2.6$ and $2.4 \leqslant \Omega_i t \leqslant 2.75$ respectively. Panels (b) and (c) plot the time evolutions of the kinetic energy $\varepsilon/m_e c^2$ of electon 3 and electron 4 respectively.

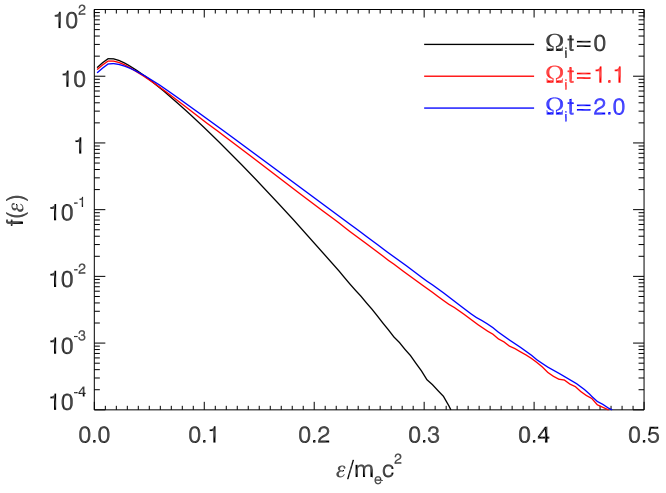

Figure 12. Electron energy spectrum computed in the whole simulation domain at $\Omega_i t = 0$, 1.1, and 2.0.

where they gyrate in a semi-circle, and then leave. During the semi-circle gyration, these electrons are accelerated by the inductive electric field in the pileup region.

The Weibel instability (or filamentation instability) has been found to play an important role in the hot, dense plasmas produced by high-intensity ($\geqslant 10^{18}$ W cm^{-2}), picosecond- or femtosecond-duration laser pulses [51–53]. The development of the counter-streaming Weibel instability leads to the generation of the turbulent magnetic fields in the plasmas. On the other hand, in laser-driven magnetic reconnection experiments, the laser beams are nanosecond-duration, and their intensity is $10^{14} - 10^{15}$ W cm^{-2}. In the nanosecond-pulse regime, we have demonstrated that the Weibel instability also develops due to the electron temperature anisotropy. Therefore, a turbulent/wavy magnetic structure is also generated at the edges of the magnetic ribbons. The turbulent/wavy magnetic structure may have a significant effect on the reconnection onset.

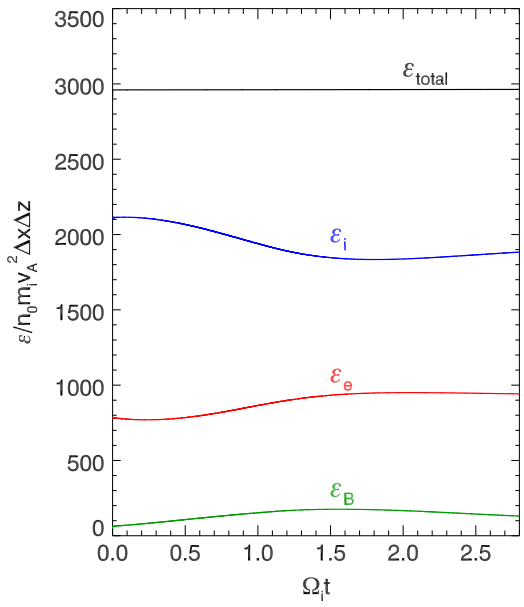

Figure 13. Time evolutions of total energy ε_{total}, ion and electron kinetic energies ε_i, ε_e, and magnetic energy ε_B. The total energy $\varepsilon_{total} = \varepsilon_i + \varepsilon_e + \varepsilon_B + \varepsilon_E$. Here ε_E is the energy of the electric field which is very small and thus negligible.

Magnetic reconnection between laser-produced plasma bubbles is found to be in a strongly driven reconnection regime. Fox *et al* [44, 45] have demonstrated that the upstream magnetic flux pileup plays an essential role in the sharply increase of the reconnection rate in the laser-driven magnetic reconnection. In the present study, we have further shown that the magnetic flux pileup is also very important for the electron energization. Before magnetic reconnection begins, the upstream electrons are pre-energized through betatron acceleration. These pre-energized electrons are easier to get further energized during magnetic reconnection [16]. As the two expanding plasma bubbles approach to and squeeze each other, a thin current sheet forms between them [46]. The electrons in the current sheet can also be pre-energized by reflections between the two bubbles, which is a Fermi-like process. Therefore, the current sheet is thermalized, corresponding to a high-beta magnetic reconnection which has a low efficiency at converting magnetic energy into the electron kinetic energy [54]. This is why the electron energization by magnetic reconnection is less significant than the enegization by the magnetic flux pileup and plasma bubble expansion.

Acknowledgments

This work was supported by 973 Program (2013CBA01503, 2012CB825602), the National Science Foundation of China, Grant Nos. 41474125, 41331067, 11235009, 41174124, 41274144, 41121003, CAS Key Research Program KZZD-EW-01-4, and the Specialized Research Fund for State Key Laboratories of China.

References

[1] Biskamp D 2000 *Magnetic Reconnection in Plasmas* (Cambridge: Cambridge University Press)
[2] Birn J and Priest E R 2007 *Reconnection of Magnetic Fields: Magnetohydrodynamics and Collisionless Theory and Observations* (Cambridge: Cambridge University Press)
[3] Yamada M, Kulsrud R and Ji H T 2010 *Rev. Mod. Phys.* **82** 603
[4] Giovanelli R G 1946 *Nature* **158** 81
[5] Tsuneta S 1996 *Astrophys. J.* **456** 840
[6] Su Y, Veronig A M, Holman G D, Dennis B R, Wang T J, Temmer M and Gan W Q 2013 *Nat. Phys.* **9** 489
[7] Baker D N, Pulkkinen T I, Angelopoulos V, Baumjohann W and McPherron R L 1996 *J. Geophys. Res.* **101** 12975
[8] Nagai T, Fujimoto M, Saito Y, Machida S, Terasawa T, Nakamura R, Yamamoto T, Mukai T, Nishida A and Kokubun S 1998 *J. Geophys. R* **103** 4419
[9] Angelopoulos V *et al* 2008 *Science* **321** 931
[10] Wesson J A 1990 *Nucl. Fusion* **30** 2545
[11] Yamada M, Levinton F M, Pomphrey N, Budny R, Manickam J and Nagayama Y 1994 *Phys. Plasmas* **1** 3269
[12] Øieroset M, Lin R P, Phan T D, Larson D E and Bale S D 2002 *Phys. Rev. Lett.* **89** 195001
[13] Wang R S, Lu Q M, Huang C and Wang S 2010 *J. Geophys. Res.* **115** A01209
[14] Fu H S, Khotyaintsev Y V, Vaivads A, Retinò A and André M 2013 *Nat. Phys.* **9** 426
[15] Pritchett P L 2006 *J. Geophys. Res.* **111** A10212

[16] Huang C, Lu Q M and Wang S 2010 *Phys. Plasmas* **17** 072306
[17] Egedal J, Daughton W and Le A 2012 *Nat. Phys.* **8** 321
[18] Fu X R, Lu Q M and Wang S 2006 *Phys. Plasmas* **13** 012309
[19] Pritchett P L 2006 *Geophys. Res. Lett.* **33** L13104
[20] Hoshino M, Mukai T, Terasawa T and Shinohara I 2001 *J. Geophys. Res.* **106** 25979–97
[21] Fermi E 1949 *Phys. Rev.* **75** 1169
[22] Brown J C and Hoyng P 1975 *Astrophys. J.* **200** 734
[23] Drake J F, Swisdak M, Che H and Shay M A 2006 *Nature* **443** 553
[24] Guo F, Li H, Daughton W and Liu Y H 2014 *Phys. Rev. Lett.* **113** 155005
[25] Fu H S, Khotyaintsev Y V, André M and Vaivads A 2011 *Geophys. Res. Lett.* **38** L16104
[26] Wu M Y, Lu Q M, Volwerk M, Vörös Z, Zhang T L, Shan L C and Huang C 2013 *J. Geophys. Res.* **118** 4804–10
[27] Huang C, Wu M Y, Lu Q M, Wang R S and Wang S 2015 *J. Geophys. Res.* **120** 1759–65
[28] Yamada M, Ono Y, Hayakawa A, Katsurai M and Perkins F 1990 *Phys. Rev. Lett.* **65** 721
[29] Yamada M, Perkins F, MacAulay A, Ono Y and Katsurai M 1991 *Phys. Fluids* B **3** 2379
[30] Brown M R 1999 *Phys. Plasmas* **6** 1717
[31] Brown M R, Cothran C D and Fung J 2006 *Phys. Plasmas* **13** 056503
[32] Yamada M, Ji H T, Hsu S, Carter T, Kulsrud R, Bretz N, Jobes F, Ono Y and Perkins F 1997 *Phys. Plasmas* **4** 1936
[33] Yamada M, Ren Y, Ji H T, Breslau J, Gerhardt S, Kulsrud R and Kuritsyn A 2006 *Phys. Plasmas* **13** 052119
[34] Egedal J, Fasoli A, Porkolab M and Tarkowski D 2000 *Rev. Sci. Instrum.* **71** 3351
[35] Egedal J, Øieroset M, Fox W and Lin R P 2005 *Phys. Rev. Lett.* **94** 025006
[36] Li C K, Seguin F H, Frenje J A, Rygg J R, Petrasso R D, Town R P J, Landen O L, Knauer J P and Smalyuk V A 2007 *Phys. Rev. Lett.* **99** 055001
[37] Rosenberg M, Li C K, Fox W, Igumenshchev I, Séguin F, Town R P J, Frenje J, Stoeckl C, Glebov V and Petrasso R 2015 *Nat. Commun.* **6** 6190
[38] Nilson P M *et al* 2006 *Phys. Rev. Lett.* **97** 255001
[39] Nilson P M *et al* 2008 *Phys. Plasmas* **15** 092701
[40] Willingale L *et al* 2010 *Phys. Plasmas* **17** 043104
[41] Stamper J A, McLean E A and Ripin B H 1978 *Phys. Rev. Lett.* **40** 1177
[42] Dong Q L *et al* 2012 *Phys. Rev. Lett.* **108** 215001
[43] Lu S, Lu Q M, Huang C, Dong Q L, Zhu J Q, Sheng Z M, Wang S and Zhang J 2014 *New J. Phys.* **16** 083021
[44] Fox W, Bhattacharjee A and Germaschewski K 2011 *Phys. Rev. Lett.* **106** 215003
[45] Fox W, Bhattacharjee A and Germaschewski K 2012 *Phys. Plasmas* **19** 056309
[46] Lu S, Lu Q M, Dong Q L, Huang C, Wang S, Zhu J Q, Sheng Z M and Zhang J 2013 *Phys. Plasmas* **20** 112110
[47] Pritchett P L 2001 *J. Geophys. Res.* **106** 3783–98
[48] Dorfman S, Daughton W, Roytershteyn J H, Ren Y and Yamada M 2008 *Phys. Plasmas* **15** 102107
[49] Weibel E S 1959 *Phys. Rev. Lett.* **2** 83
[50] Krall N A and Trivelpiece A W 1973 *Principle of Plasma Physics* (New York: McGraw-Hill)
[51] Califano F, Sarto D D and Pegoraro F 2006 *Phys. Rev. Lett.* **96** 15008
[52] Mondal S *et al* 2012 *Proc. Natl Acad. Sci.* **109** 8011
[53] Fox W, Fiksel G, Bhattacharjee A, Chang P Y, Germaschewski K, Hu S X and Nilson P M 2013 *Phys. Rev. Lett.* **111** 225002
[54] Li X, Guo F, Li H and Li G 2015 *Phys. Rev. Lett.* **811** L24